

TOWARD FLUOROSCOPIC SHAPE RECONSTRUCTION FOR CONTROL OF STEERABLE MEDICAL DEVICES

Jessica Burgner

Department of Mechanical Engineering
Vanderbilt University
Nashville, Tennessee, 37212
jessica.burgner@vanderbilt.edu

S. Duke Herrell

Department of Urologic Surgery
Vanderbilt University Medical Center
Nashville, Tennessee, 37212
duke.herrell@vanderbilt.edu

Robert J. Webster III

Department of Mechanical Engineering
Vanderbilt University
Nashville, Tennessee, 37212
robert.webster@vanderbilt.edu

ABSTRACT

Control of surgical continuum robot manipulators and steerable needles requires accurate real-time sensing of tip position and/or shaft shape. Medical image feedback provides the most straightforward and widely available method of measuring device and clinical target positions and shapes during insertion or tissue manipulation. In this paper we present a method for automatic robot/needle curve segmentation from fluoroscopic images, as well as a method for 3D reconstruction of the curve using biplane fluoroscopy images.

INTRODUCTION

It is desirable to develop surgical robotic manipulators that are as slender as possible while retaining the necessary structural robustness and dexterity (see [1–4] for examples of continuum manipulators). It is also desirable to actively steer needles through curved paths during insertion [5, 6], and to control actively bending catheters [7].

A common challenge in controlling all of the above robots and devices is sensing their configuration, i.e. determining the actual robot shape. While magnetic tracking and optical fiber-based techniques may be possible, the sensors used themselves will consume valuable space within the device. However, medical imaging is almost always available when such devices are used clinically. Fluoroscopy (video X-ray) specifically is a widely available imaging technology that is appealing for shape sensing and ultimately enabling control of these continuum devices. Applications of intraoperative fluoroscopic imaging for shape sensing include biplane tracking of catheter guide-wires [8, 9] and image-guided needle steering based on single plane fluoroscopy images [10, 11].

Our initial work in shape sensing from using stereo camera images used a computationally expensive self-organizing maps algorithm [12]. In this paper we propose an alternative method for shape sensing using computationally efficient filters for segmentation of the robot in individual images and epipolar geometry for 3D shape reconstruction.

METHODS

Segmentation of Robot From Individual Images

Fluoroscopy provides greyscale images (see Figure 2). As a first step toward reconstruction of the robot space curve from two projections, we begin with extracting the robot shape in individual images.

Initially, the image is preprocessed with a low-pass filter using a pixel-wise adaptive Wiener method based on statistics estimated from a local 6×6 neighborhood of each pixel. For filtering the robot shape, we adapted the vessel filter introduced by Frangi et al. [13], who proposed a multi scale filter based on the second order derivative information (Hessian) of a Gaussian kernel.

The eigenvalue decomposition of the Hessian matrix directly gives the direction of the smallest curvature, which is along the robot. This method avoids application of several filters in multiple directions. Pixels belonging to the continuum robot have one very small eigenvalue and one very large eigenvalue.

The 2D roundness R accounting for the eccentricity of the second order ellipse, and the measure for the second order structureness S [13] are respectively given by,

$$R = \lambda_1 / \lambda_2 \quad \text{and} \quad S = \lambda_1^2 + \lambda_2^2 \quad (1)$$

The 2D continuum robot filter function is then defined in

accordance to Frangi’s 2D vesselness function,

$$\vartheta_0 = \begin{cases} 0, & \text{if } \lambda_2 < 0 \\ \exp(-R^2/\beta_1) \cdot (1 - \exp(-S/\beta_2)), & \text{else} \end{cases} \quad (2)$$

with $\beta_1 = 2 \cdot 0.8^2$ and $\beta_2 = 2 \cdot (\max(I)/4)^2$ controlling the sensitivity of R and S , where $\max(I)$ is the maximum intensity in the image.

The filtered image is thresholded by the mean intensity in order to obtain a binary image for further processing. Applying a morphological thinning operator allows extraction of the robot’s backbone from the thinned binary image. We thin all objects in the binary image to lines [14]. The thresholded image may contain shape fragments not necessarily belonging to the robot, e.g. from very dark edges of organs. To overcome this false detection, we evaluate the size of connected pixel regions in the thinned image. Groups of connected pixels that are not large enough to be the robot (below a certain threshold based on the expected length of the robot in the image) are removed from consideration. The robot’s shape is then represented by evenly distributed points along the backbone with a user-defined spacing parameter in pixels, which should be set according to the application.

Shape Reconstruction

The automatic shape segmentation algorithm is applied on two corresponding fluoroscopy images, acquired at distinct poses. This produces evenly distributed control points along the robot’s backbone for both images and allows application of epipolar geometry for determination of point correspondences, as a step towards three-dimensional curve reconstruction.

Given a pair of images, for each point (u, v) in the first image, a corresponding point (u', v') exists in the second image, which lies on the epipolar line for (u, v) . The mapping from a point in one image to the corresponding epipolar line in the other image is represented by the fundamental matrix, which can be derived algebraically given the two camera projection matrices [15].

We assume that the camera calibration matrix for the X-ray source is known, i.e. the intrinsic parameters. We neglect distortion under the assumption the system has been calibrated to account for it, or (as is the case of our biplane system described later) that we have flat-panel detectors. Further, we assume that the extrinsic camera parameters are known, which can be determined from the fluoroscopy system itself (i.e. either it is encoded or an image-based stereo calibration has been performed using fiducial markers visible in both projections).

For each segmented robot control point in one fluoroscopy image, we determine the epipolar line in the other image. By intersecting the epipolar line with the segmented robot in the other image, point correspondences are determined. For reconstructing the 3d points for the established point correspondences, we apply a projective-invariant triangulation method as described

in [15], i.e. we estimate the 3d point for each corresponding image point pair by minimizing the reprojection error using Newton’s method.

Since it does not matter which image we consider the initial image, we can obtain a second estimate of the space curve of the robot by starting with the opposite image and repeating the procedure above. We do this, and use the resulting information to apply a plausibility measure. This helps to account for cases where (due to e.g. partial occlusion of the robot due to non-optimal acquisition angles) incorrect or no corresponding point is determined for a given control point. Our plausibility measure is as follows:

$$\max(\kappa_1) \leq \epsilon \quad \text{and} \quad \max(\kappa_2) \leq \epsilon \quad (3)$$

with κ_1 and κ_2 being the curvature values of the curve reconstruction segments obtained from the two images and ϵ a user-defined parameter. We chose ϵ to be the product of the spacing between control points (in pixels) and the resolution of the image in mm per pixel. If this condition is not fulfilled, the reconstruction led to an incorrect space curve and is rejected.

Image Acquisition

In order to evaluate the accuracy of the segmentation algorithm we have developed, we acquired biplane fluoroscopy images (Allura Xper FD20/20, Philips Medical Systems) of a tissue-mimicking anthropomorphic phantom of a human liver with internal vessel-like structures and tumors, which was made using silicon rubber (Dragon Skin, Smooth-On, Inc. Easton, PA). A two-tube active cannula was inserted into the phantom (see Figure 1). The acquired images were 1024×1024 greyscale



Figure 1. Acquisition of biplane fluoroscopy images from a two-tube active cannula in an anthropomorphic liver phantom.

with a native pixel size of $308\ \mu\text{m}$.

Since there is no ground-truth curve to compare our 3d reconstruction results from biplane images, we also developed simulation software utilizing the Visualization Toolkit (vtk, Kitware Inc.). Our software allows arbitrary setup of two virtual camera views with respect to a known ground-truth continuum robot curve (a 3D spline with a tube filter of user-defined radius). In the simulation, the focal length, view angle, and image size were chosen to correspond with the real biplane fluoroscopy system. In order to simulate imperfect image capture in fluoroscopy images properly, exported greyscale images are blurred with a 5×5 Gaussian kernel and Gaussian white noise is added with zero mean and 0.002 variance. The resulting images are visually comparable to fluoroscopy images.

RESULTS

Segmentation

The segmentation method described in the previous Section was implemented in Matlab using the Image Processing Toolbox. We ran the segmentation algorithm on ten fluoroscopy images of a cannula inserted into a liver phantom, obtained using the biplane fluoroscopy system described in the previous Section. Figure 2 shows three exemplary input and segmentation result images. We evaluated the automatically determined tip position in comparison to a manually identified tip point. The mean tip offset was 1.55 pixels.

3D Reconstruction Simulation with Ground Truth

We analyzed the 3D reconstructions of ten known, ground truth continuum robot curves in simulated fluoroscopy images under the same acquisition settings obtained with the software described in the previous Section. The continuum robots had a radius of 0.6 mm and the lengths varied between 67 mm and 188 mm with an average at 130.6 mm. The images had a resolution of 1024×1024 pixels with 0.523 mm/pixel resolution in x- and y-directions. The robot had a known shape (3d spline curve), which was used as ground truth for comparison with the 3d reconstruction results.

We evaluated the mean closest point distance of the reconstructed space curves to the ground truth curve. The mean error for all ten robot configurations was 0.24 ± 0.023 mm with a maximum error of 0.264 mm. Further, we compared the length of the reconstructed robot with the length of the ground truth robot curves. The mean error for all ten robot configurations was 0.473 ± 0.353 mm with a maximum error of 1.075 mm. Additionally, we evaluated the Cartesian distance between the reconstructed robot tip position and the ground truth tip position. The mean error was 0.617 ± 0.230 mm. The maximum tip offset was 1.021 mm.

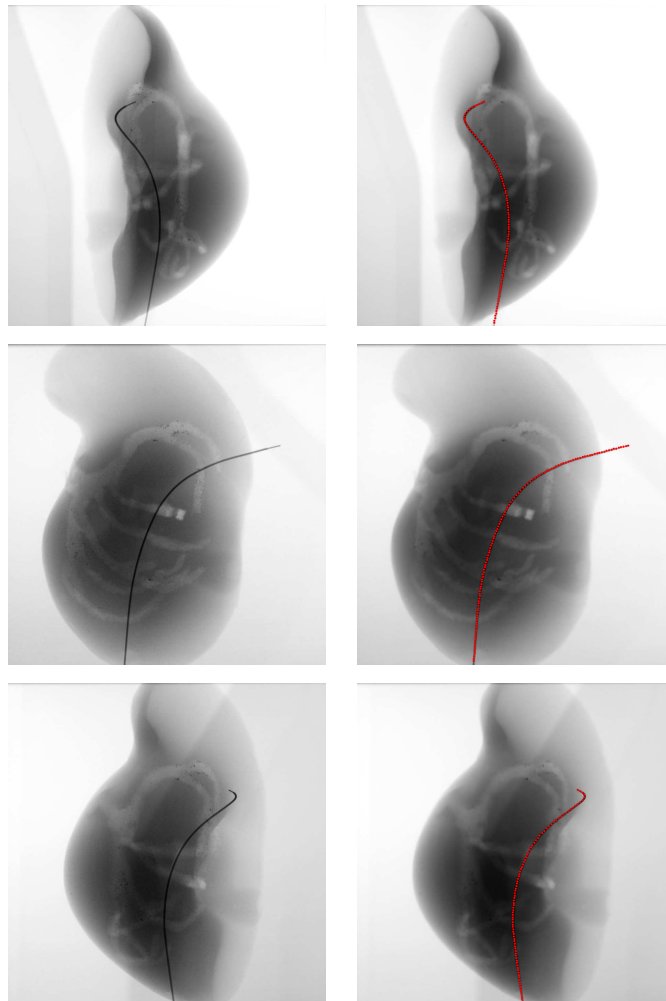


Figure 2. Input images and corresponding segmentation results.

CONCLUSION

The contribution of this paper is a method for automatic image segmentation and 3D reconstruction of the shape of a flexible, curved, medical robot. Such sensing represents an initial step towards closed-loop control of these devices, which is required in many medical applications. Future work will involve integrating our algorithm into a closed-loop control system. We also note that it will be possible to enhance the efficiency of our reconstruction algorithm if a kinematic model of the robot is available, even if the robot is deformed somewhat by the surrounding tissue medium, and we intend to investigate this in future work. We foresee many future applications of the techniques introduced in this paper in interventions such as brachytherapy, thermal tumor ablation, and kidney stone removal, among many others.

REFERENCES

- [1] Camarillo, D. B., Milne, C. F., Carlson, C. R., Zinn, M. R., and Salisbury, J. K., 2008. “Mechanics Modeling of Tendon-Driven Continuum Manipulators”. *IEEE Transactions on Robotics*, **24**(6), pp. 1262–1273.
- [2] Simaan, N., Xu, K., Kapoor, A., Wei, W., Kazanzides, P., Flint, P., and Taylor, R., 2009. “Design and Integration of a Telerobotic System for Minimally Invasive Surgery of the Throat.”. *The International Journal of Robotics Research*, **28**(9), pp. 1134–1153.
- [3] Rucker, D. C., Jones, B. A., and Webster III, R. J., 2010. “A Geometrically Exact Model for Externally Loaded Concentric-Tube Continuum Robots”. *IEEE Transactions on Robotics*, **26**(5), pp. 769–780.
- [4] Dupont, P. E., Lock, J., Itkowitz, B., and Butler, E., 2010. “Design and Control of Concentric-Tube Robots”. *IEEE Transactions on Robotics*, **26**(2), pp. 209–225.
- [5] Webster, R. J., Kim, J. S., Cowan, N. J., Chirikjian, G. S., and Okamura, A. M., 2006. “Nonholonomic Modeling of Needle Steering”. *The International Journal of Robotics Research*, **25**(5-6), pp. 509–525.
- [6] Reed, K. B., Majewicz, A., Kallem, V., Alterovitz, R., Goldberg, K., Cowan, N. J., and Okamura, A. M., 2010. “Robot-Assisted Needle Steering”. *IEEE Robotics & Automation Magazine*.
- [7] Fu, Y., Liu, H., Huang, W., Wang, S., and Liang, Z., 2009. “Steerable catheters in minimally invasive vascular surgery”. *The International Journal of Medical Robotics and Computer Assisted Surgery*, **5**(4), pp. 381–91.
- [8] Baert, S. A. M., van de Kraats, E. B., van Walsum, T., Viergever, M. A., and Niessen, W. J., 2003. “Three-dimensional guide-wire reconstruction from biplane image sequences for integrated display in 3-D vasculature”. *IEEE Transactions on Medical Imaging*, **22**(10), pp. 1252–8.
- [9] Lessard, S., Lau, C., Chav, R., Soulez, G., Roy, D., and de Guise, J. A., 2010. “Guidewire tracking during endovascular neurosurgery.”. *Medical engineering & physics*, **32**(8), pp. 813–21.
- [10] Glozman, D., and Shoham, M., 2007. “Image-Guided Robotic Flexible Needle Steering”. *IEEE Transactions on Robotics*, **23**(3), pp. 459–467.
- [11] Wang, P., Marcus, P., Chen, T., and Comaniciu, D., 2010. “Using needle detection and tracking for motion compensation in abdominal interventions”. In *IEEE International Symposium on Biomedical Imaging: From Nano to Macro*, IEEE, pp. 612–615.
- [12] Croom, J. M., Rucker, D. C., Romano, J. M., and Webster III, R. J., 2010. “Visual Sensing of Continuum Robot Shape Using Self-Organizing Maps”. *IEEE International Conference on Robotics and Automation*, pp. 4591–4596.
- [13] Frangi, A., Niessen, W., Vincken, K., and Viergever, M., 1998. “Multiscale Vessel Enhancement Filtering”. In *Medical Image Computing and Computer-Assisted Intervention*, pp. 130–137.
- [14] Lam, L., Lee, S.-W., and Suen, C., 1992. “Thinning methodologies—a comprehensive survey”. *IEEE Transactions on Pattern Analysis and Machine Intelligence*, **14**(9), pp. 869–885.
- [15] Hartley, R., and Zisserman, A., 2000. *Multiple View Geometry in Computer Vision*, 2nd ed. Cambridge University Press.